Femtosecond MeV Electron Energy-Loss Spectroscopy

R. K. Li* and X. J. Wang

SLAC National Accelerator Laboratory, 2575 Sand Hill Road, Menlo Park, California 94025, USA

(Received 31 August 2017; published 9 November 2017)

Pump-probe electron energy-loss spectroscopy (EELS) with femtosecond temporal resolution will be a transformative research tool for studying nonequilibrium chemistry and electronic dynamics of matter. In this paper, we propose a concept of femtosecond EELS utilizing mega-electron-volt electron beams from a radio-frequency (rf) photocathode source. The high acceleration gradient and high beam energy of the rf gun are critical to the generation of 10-fs electron beams, which enables an improvement of the temporal resolution by more than 1 order of magnitude beyond the state of the art. In our proposal, the "reference-beam technique" relaxes the energy stability requirement of the rf power source by roughly 2 orders of magnitude. The requirements for the electron-beam quality, photocathode, spectrometer, and detector are also discussed. Supported by particle-tracking simulations, we demonstrate the feasibility of achieving sub-electron-volt energy resolution and approximately 10-fs temporal resolution with existing or near-future hardware performance.

DOI: 10.1103/PhysRevApplied.8.054017

I. INTRODUCTION

Electron energy-loss spectroscopy (EELS) analyzes the energy distribution of initially monoenergetic electrons after they have interacted with a specimen [1,2]. The change in kinetic energy of electrons carries rich information about the chemistry and electronic structures of the specimen atoms, which reveals the details of the bonding and valence states, the nearest-neighbor structures, the dielectric response, the band gap, etc. The EELS measurement combined with diffraction in reciprocal space and imaging in real space using modern electron microscopes provide a multidimensional panorama of material properties.

An exciting development of modern science focuses on the dynamics of material properties in nonequilibrium, such as heating, phase transitions, and chemical reactions in addition to those in steady states [3–6]. X-ray [7–9] and electron [10–18] instruments and techniques with ever-improving temporal resolution, as well as spatial and energy resolutions are being developed to visualize these processes, aiming to fully understand the connections between structures, dynamics, and functionality, and ultimately, controlling energy and matter.

Time-resolved EELS measurements have recently been carried out in ultrafast electron microscopes (UEMs), which showcased their unique capabilities of mapping, for example, ultrafast electronic dynamics in solids and coherent quantum manipulation of free electrons in the optical near field [19–24]. The technique, which is complementary to spectroscopy measurement using x-ray free-electron lasers (XFELs), is well suited for very thin samples due to the much stronger interaction of electrons with material. Also, in principle, the probe size of electron beams can be focused by electromagnetic lenses to nanometer or smaller to provide detailed mapping of materials on atomic scales.

Existing UEM instruments are based on modifying commercial transmission electron microscopes to operate with pulsed photoemitted electron beams, instead of the conventional continuous-wave thermionic or field emission. It is highly challenging to reach desired energy and temporal resolutions in time-resolved EELS measurements, i.e., to minimize the energy spread and bunch length of electron beams simultaneously, which can both be severely degraded by electron-electron (e-e) interactions. The solution is to operate these instruments with extremely low charge density—on average, a single electron per pulse—to eliminate the effects of e-e interactions. The typical energy resolution of this operation mode is 1–2 eV [19–21,23,24]. The temporal resolution, however, is still limited to several hundred femtoseconds, which are dominated by the pulse duration of the photoelectron beams. The photoelectrons are generated with a few tenths of an electron volt initial energy spread, which translates into several-hundred-femtosecond pulse duration due to vacuum dispersion [22,24], while at least 1-order-of-magnitude shorter bunch length is desired to capture fast dynamics of electronic structures.

To tackle the challenge associated with vacuum dispersion, an electron source with a significantly higher acceleration gradient and higher output energy is necessary. Radio-frequency (rf) photocathode guns featuring 10-s to 100-MV/m gradient and several MeV beam energy are the ideal choice. Recently, these sources have been optimized for ultrafast electron diffraction [25–38] and imaging [39–41]

*Corresponding author.
lrk@slac.stanford.edu

with transformative impacts by delivering unprecedented temporal and reciprocal- or real-space resolutions. Unfortunately, the energy stability of the electron beams from rf guns determined by the stability of the driving rf power sources is currently at best at the 1×10^{-5} level, i.e., 50 eV for 5-MeV beams, which is far from adequate for spectroscopy applications. Thus, unless some technical breakthrough can improve the rf stability by at least 2 orders of magnitude, it is regarded impractical to consider photocathode rf guns for femtosecond EELS.

Here, we propose a "reference-beam technique" that significantly relaxes the demanding requirement of the rf stability, and we demonstrate the feasibility of femtosecond MeV EELS based on rf photocathode electron sources. We present a complete conceptual design of a femtosecond MeV EELS system. Detailed simulation results show that one can achieve sub-electron-volt energy resolution even with 50-eV beam energy fluctuation. Meanwhile, the temporal resolution is improved to the 10-fs level, which is more than 1 order of magnitude beyond the state of the art. One may also take advantage of the MeV beam energy to study thicker samples due to the reduced inelastic cross section compared to commonly used (200–300)-keV electrons. Or, for the same sample thickness, there is reduced multiple scattering with MeV electrons, which significantly simplifies the interpretation of the EELS spectrum.

In this paper, we first introduce the concept of the reference-beam technique and the overall system design in Sec. II. The temporal resolution, which includes contributions from the electron-beam pulse duration and pump-to-probe time-of-arrival jitter, is evaluated in Sec. III. Impacts of the gun rf field on the energy resolution are presented in Sec. IV. We discuss the requirements of the spectrometer resolution and transverse beam qualities in Sec. V. The effects of *e-e* interaction on the energy resolution are discussed in Sec. VI.

II. REFERENCE-BEAM CONCEPT FOR FEMTOSECOND MeV EELS

We illustrate in Fig. 1 the concept of the reference-beam technique for femtosecond MeV EELS based on a rf photocathode electron source. Two electron beams, which are called the probe beam and reference beam, are generated from the photocathode with both transverse (approximately 100 μm) and longitudinal (time approximately 1 ps) separations. The energies of both electron beams fluctuate at the 50-eV level (1×10^{-5} of 5 MeV) due to the stability of the rf power source. However, the *difference* between their energies and the energy spread of each individual beam can all be controlled at the sub-0.1-eV level. Detailed analysis of the contribution from the gun rf field and *e-e* interactions is presented in Secs. IV and VI, respectively.

At the sample location, the two beams are also transversely (vertically) separated, and only the probe beam interacts with the sample. The longitudinal separation is necessary to minimize *e-e* interactions at transverse focus along the beam line. A high-resolution spectrometer measures the energy of both the scattered probe beam and the unperturbed reference beam. The energy difference between the two beams consists of two parts: (1) the energy loss due to the sample and (2) the original energy difference when the sample is not present. By recording the probe- and reference-beam pair on shot-by-shot basis and comparing the energy difference, one can construct a complete energy-loss spectrum due to the sample. Note that the original energy difference contributes as a fixed offset of the zero-loss peak and does not distort of the energy axis of the spectrum. A detector operating in electron-counting mode is used to record the electron-beam pairs. Multiple pump-probe events are repeated and combined to build up the statistics of the spectrum until the signal-to-noise ratio in the interested spectrum regions normalized to the zero-loss peak and the reference beam is adequate for tracking laser-excited dynamics.

The energy resolution of the reference-beam technique is

$$\Delta E^2 = (E_{\text{probe}} - E_{\text{ref}})^2 + \delta E_{\text{probe}}^2 + (\sigma/D)^2, \qquad (1)$$

where $E_{\text{probe|ref}}$ is the average energy of the probe or reference beam, and δE_{probe} is the energy spread of the probe beam. Note that the energy spread of the reference beam does not contribute here since only its average energy is relevant. σ/D is the instrumentation energy resolution

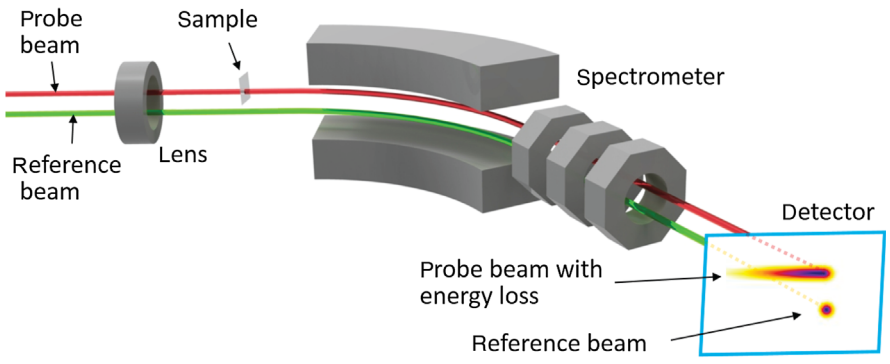

FIG. 1. Concept of the reference-beam technique for femtosecond MeV EELS based on rf photocathode guns.

of the spectrometer, where σ is the beam spot size on the spectrometer detector, and D is the spectrometer dispersion. To ensure that σ/D is also well below 0.1 eV, with a practical spectrometer design, σ should be less than a few tens of nanometers on the sample. Combined with the requirement of the beam divergence, which should be much smaller than the typical Bragg angle of 1 mrad for 5-MeV electrons, the normalized beam emittance should be sub-nanometer-rad.

The success of femtosecond MeV EELS relies on the generation and preservation of sub-electron-volt energy spread, 10-fs bunch length, and sub-nanometer emittance electron beams from the source, through the sample, till the spectrometer. Such a precisely shaped and miniature phase-space volume can accommodate only a single electron per pulse, as we show in Sec. VI. A high-repetition-rate electron source is a natural choice to build up high signal-to-noise ratio within a reasonable data acquisition time. In the circumstances where the pump-probe repetition rate is limited to kilohertz due to laser-induced sample heating, a pulsed rf gun is also an option with >100-MV/m acceleration gradient to deliver the shortest possible electron-beam pulse durations. The simulation results presented in the following sections are based on the design of a 200-MHz quarter-wave-resonator-type superconducting rf (SRF) gun.

A more technical schematic of the system is shown in Fig. 2, which includes a rf gun, a condenser lens, a high-resolution spectrometer, etc. The design and consideration of each key component, as well as the control and evolution of the electron beams, are discussed in the following sections.

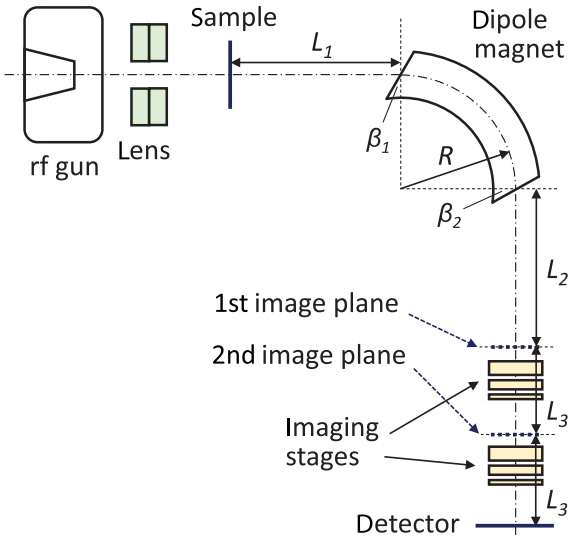

FIG. 2. Schematic of the femtosecond MeV EELS system. Components include a rf gun, a condenser lens, the sample, and a spectrometer. The spectrometer consists of a dipole magnet and two stages of magnifying imaging lenses.

III. TEMPORAL RESOLUTION: BUNCH LENGTH AND TIME-OF-ARRIVAL JITTER

In a pump-probe EELS measurement, a pump-laser pulse first illuminates the sample and prepares the system to an excited state. After a controlled time delay, a probe electron beam interacts with the samples and captures the transient electronic property. By repeating the pump-probe events at various time delays, one can reconstruct the full evolution of the dynamic process. The temporal resolution of the measurement is

$$\tau = (\tau_e^2 + \tau_{\text{pump}}^2 + \tau_{\text{TOA}}^2 + \tau_{\text{VM}}^2)^{1/2}, \tag{2}$$

where τ_e and τ_{pump} are the pulse durations of the probe electron and pump-laser pulses, respectively, τ_{TOA} is the time-of-arrival (TOA) jitter between the pump and probe pulses at the sample, and τ_{VM} is the velocity mismatch term [42]. τ_{VM} is negligible for micrometer and thinner samples.

τ_e is determined by several factors, including the longitudinal dynamics in the rf field, initial energy-spread-induced vacuum dispersion, as well as the initial pulse duration from photoemission. The longitudinal dynamics in a rf gun depends on the field strength and the launch phase when the photoelectrons are generated. The on-axis longitudinal electric field E_z of the rf gun is shown in Fig. 3. Here, we choose a launch phase for close to maximum output energy, hence, minimal rf-induced energy spread, to eventually reach high EELS energy resolution. The reason is discussed more quantitatively in Sec. IV. With this launch phase, there is no effective rf compression [43], and τ_e is dominated by the initial pulse duration and vacuum dispersion.

The initial energy distribution of photoelectrons consists of several parts, including the thermal spread due to the finite electronic temperature of the cathode, the excitation bandwidth of the cathode-driving laser, and the mismatch between the photon energy and the effective work function [44–49]. One can shift the central wavelength to minimize

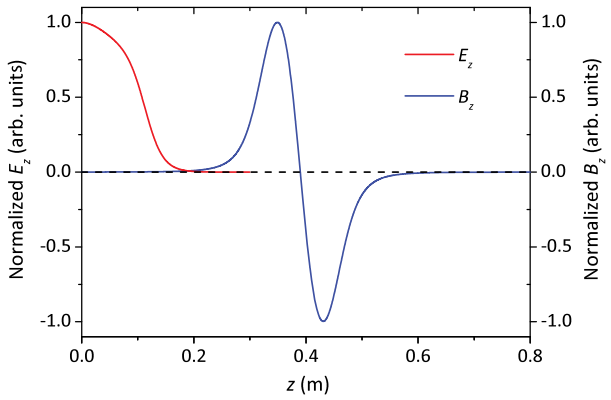

FIG. 3. On-axis longitudinal electric field E_z of the rf gun and on-axis longitudinal magnetic field B_z of the solenoid condenser lens.

the last mismatch term. The effect of laser-induced cathode heating can be controlled at a negligibly small level in our extremely low bunch charge regime [50]. In a SRF gun, the cathode temperature is well below room temperature (25 meV), and we assume the thermal spread is 5 meV rms in both transverse and longitudinal directions. The minimal value of the laser excitation bandwidth is given by the Fourier-transform limit. For a Gaussian temporal profile pulse, the FWHM excitation bandwidth is $\delta E_{\text{laser}}[\text{meV}] = 1822/\tau_{\text{laser}}[\text{fs}]$.

In order to generate short σ_e, since there is no effective rf compression and vacuum dispersion only lengthens the beam, it is important to start with short initial pulse length, and, hence, a photocathode with prompt response is highly desired. We choose metallic cathodes with a few-femtosecond response time and assume the initial pulse duration of the electron beam approximately equals that of the driving laser. On the other hand, shorter driving laser is associated with a larger, transform-limited excitation bandwidth and leads to excessive electron-beam lengthening. In Fig. 4, we show that σ_e can be optimized by adjusting τ_{laser} to balance the two competing effects. Higher rf-field gradient and beam energy can more effectively suppress vacuum dispersion and generate shorter σ_e. We perform the simulation using the GENERAL PARTICLE TRACER (GPT) code [51]. In the rest of the paper, we focus on the 50-MV/m gradient case, where σ_e is below 10 fs rms.

The other important contributing term τ_{TOA} is determined by the phase and amplitude jitters of the rf field. Here, we assume the cathode drive laser and the sample pump laser are split from a common laser pulse and, thus,

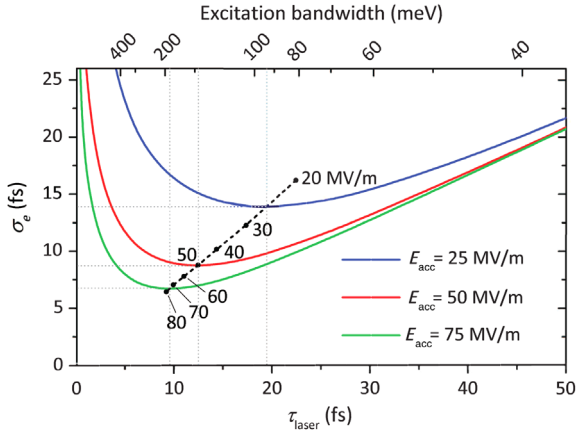

FIG. 4. The electron-beam pulse duration at the sample location σ_e can be optimized by tuning the pulse duration of the cathode-driving laser τ_{laser}. Here, we assume the initial pulse duration of the electron beam is equal to τ_{laser} with a prompt photocathode, and the initial energy spread of the electron beam includes contribution from the excitation bandwidth of a transform-limited laser. Higher rf gun gradient enables shorter minimal σ_e. The black dots indicate the minimal σ_e for gun gradient from 20 to 80 MV/m.

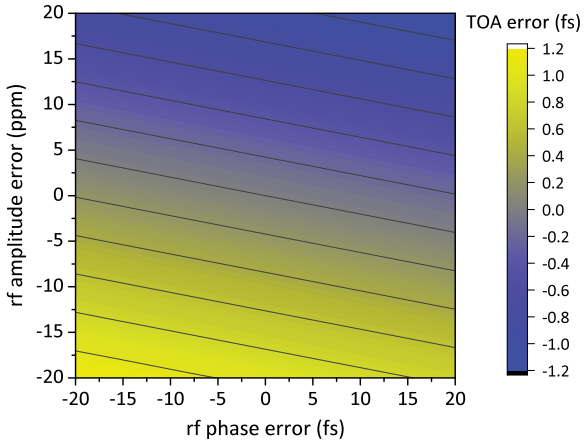

FIG. 5. TOA error between the pump-laser and probe-electron beams at the sample due to the phase and amplitude fluctuations of the gun rf field.

essentially jitter-free. The TOA error can be evaluated in a straightforward way by adding small errors in the rf amplitude and launch phase to the nominal settings. We assume that the rf amplitude and phase errors are 1×10^{-5} rms and 10 fs rms, respectively, which are typical for a state-of-the-art cw source. The TOA error stays below 1 fs within the range of $-\sigma$ to $+\sigma$ for both phase and amplitude errors, as shown in Fig. 5. Note that since at this launch phase there is minimal rf compression effect, i.e., the TOA is not sensitive to the rf phase jitter, the TOA depends more strongly on the rf amplitude fluctuation.

In this section, we quantitatively evaluate the main contributing terms to the temporal resolution and demonstrate that τ_e and τ_{TOA} can be controlled at the 10- and 1-fs levels, respectively. The pulse duration of the pump laser can be readily maintained at the 10-fs level, and the velocity mismatch term is negligible for solid-state samples, which are approximately a micrometer or thinner. Hence, we conclude that the overall temporal resolution of femtosecond MeV EELS is at the 10-fs level.

IV. rf-FIELD CONTRIBUTION TO THE ENERGY RESOLUTION

For a rf gun, due to the spatial and temporal variation of the rf electromagnetic field, the output energy of each photoelectron depends on its particular trajectory through the field. The trajectory is determined by its initial position and angle from the photocathode and the launch phase, i.e., the rf phase at the instance of photoemission. The accelerating field in the rf gun is axially symmetric around the beam axis (z axis). The longitudinal and transverse components are

$$E_z = E_{\text{acc}} e(z, r) \sin(\omega_0 t + \phi), \tag{3}$$

$$E_r = -\frac{r}{2}\frac{\partial E_z}{\partial z}, \tag{4}$$

where $E_{\rm acc}$ is the gun gradient, $e(z,r)$ is the normalized field profile, ω_0 is the resonant frequency, and ϕ is the launch phase. It is straightforward to calculate the average energy and energy spread of an electron beam for given initial spot position, spot size, divergence, and pulse duration. The main parameters are summarized in Table I.

In Fig. 6, we show the particle-tracking results for the average energy and full width 50% (FW50) energy spread of an electron beam for various initial transverse offset Δy and temporal offset Δt, with other parameters as specified in Table I. Here, Δy is defined relative to the gun center, and Δt is with respect to the launch phase for maximum output energy. Δy and Δt should be large enough such that the e-e interactions between the probe and reference beams are negligible. In Sec. VI, we discuss in detail the effects of e-e interactions, and $\Delta y = \pm 50$ μm and $\Delta t = \pm 0.5$ ps are found adequate. The probe beam and reference beam are located at $(\Delta y, \Delta t)$ and $(-\Delta y, -\Delta t)$, respectively. With these separations, the difference between the average energy of the probe and reference beams is less than 1 meV, and their energy spreads are both controlled below 0.15 eV.

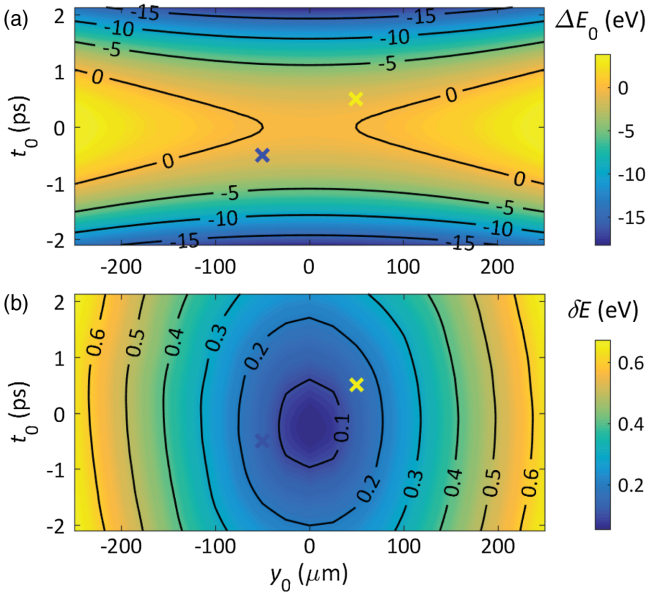

FIG. 6. Dependence of (a) the average energy and (b) FW50 energy spread of an electron beam on its initial vertical offset from the gun center Δy and temporal offset Δt from the launch phase for maximum output energy. The probe and reference beams are indicated by the yellow and blue crosses, respectively.

TABLE I. Main machine and beam parameters for femtosecond MeV EELS.

Parameters	Values
Gun gradient	50 MV/m
Gun frequency	200 MHz
Launch phase for maximum output energy	73.83°
Maximum output energy	5.12 MeV
Solenoid strength, B_0	0.40 T
Beam charge	$<1e$/pulse
Initial spot size, rms (uniform)	50 nm
Intrinsic emittance	0.23 μm/mm
Initial pulse duration, FWHM	18.2 fs
Transverse offset $\Delta y_{\rm probe\|ref}$	± 50 μm
Temporal offset $\Delta t_{\rm probe\|ref}$	± 0.5 ps
At the sample ($z = 70$ cm)	
Horizontal beam centroid $x_{0,\rm probe\|ref}$	0|0 μm
Horizontal beam size, rms $\sigma^{\rm rms}_{x,\rm probe\|ref}$	13.8|13.8 nm
Horizontal beam size, FW50 $\sigma^{\rm FW50}_{x,\rm probe\|ref}$	24.0|24.0 nm
Vertical beam centroid $y_{0,\rm probe\|ref}$	-13.8|13.8 μm
Vertical beam size, rms $\sigma^{\rm rms}_{y,\rm probe\|ref}$	13.4|13.4 nm
Vertical beam size, FW50 $\sigma^{\rm FW50}_{y,\rm probe\|ref}$	22.7|22.6 nm
Beam divergence, rms $\sigma_{x'/y',\rm probe\|ref}$	76 μrad
Normalized emittance, rms $\epsilon_{x/y,\rm probe\|ref}$	11.5 pm rad
Temporal separation $t_{0,\rm probe} - t_{0,\rm ref}$	1.0 ps
Bunch length, rms $\sigma_{t,\rm probe\|ref}$	9.2|9.4 fs
Beam energy $E_{\rm probe\|ref}$	5.12 MeV
Energy difference $E_{\rm probe} - E_{\rm ref}$	0.001 eV
Energy spread, FW50 $\delta E_{\rm probe\|ref}$	0.13|0.15 eV

The initial offsets $\pm\Delta y$ and $\pm\Delta t$, together with the rf gun and solenoid configuration, control the longitudinal and transverse separations between the probe and reference beams along the beam line. The solenoid condenser lens, as shown in Fig. 3, consists of two identical coils with opposite polarities so that the integrated rotation of the electron beams is zero as the kinetic energy stays constant through the lens. In Fig. 7, we show the longitudinal and transverse separations, as well as the transverse beam size from the photocathode to the sample location ($z = 0.7$ m). The temporal separation stays constant at 1 ps since the relative longitudinal particle motion is essentially frozen. The two beams are 27.6 μm apart in the y direction at the sample location, and only the probe beam interacts with the sample. The sample plane is imaged to the spectrometer detector with a total magnification of 16×16 times in the dispersion (x) direction and 4×4 times in the y direction. The design of the spectrometer is discussed in Sec. V.

Because of the timing error of the rf launch phase relative to the cathode-driving laser Δt_ϕ, the temporal offsets of the probe and reference beams become $\Delta t_\phi + \Delta t$ and $\Delta t_\phi - \Delta t$, respectively, which leads to a difference between their average energies. The dependence of the energy difference $E_{\rm probe} - E_{\rm ref}$ on the rf phase error, as well as on the rf amplitude error, is shown in Fig. 8. It is evident that the energy difference is insensitive to the rf amplitude fluctuation. These results quantitatively demonstrate the effectiveness of the reference-beam technique. With assumed specifications of 10 fs rms rf phase error and 1×10^{-5} rms

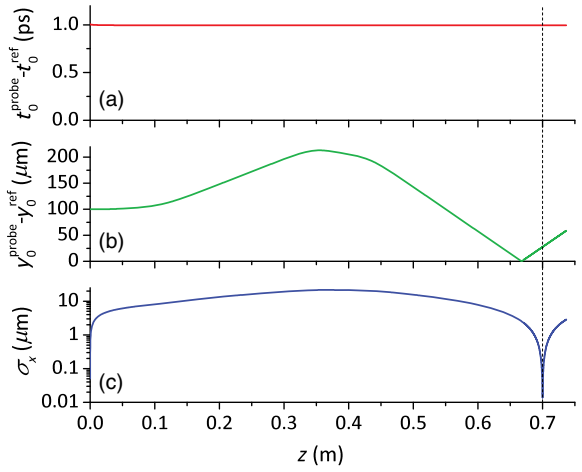

FIG. 7. The (a) longitudinal (temporal) and (b) transverse separations between the probe and reference beams, as well as the (c) rms transverse beam size from the photocathode ($z = 0$ m) to the sample location ($z = 0.7$ m).

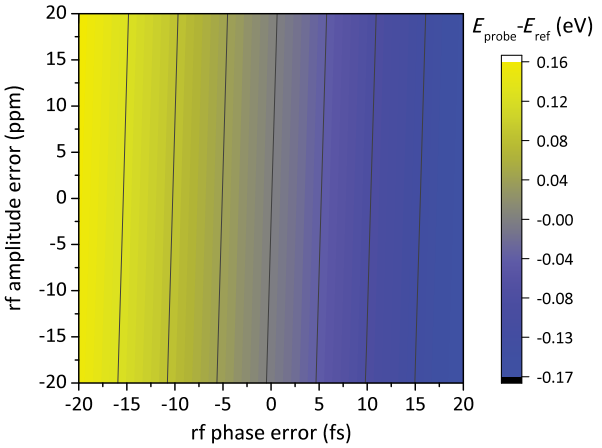

FIG. 8. Dependence of the energy difference between of the probe and reference beams $E_{\text{probe}} - E_{\text{ref}}$ on the phase and amplitude errors of the gun rf field. The rf phase and amplitude fluctuations are 10 fs rms and 1×10^{-5} rms, respectively.

amplitude error, the uncertainty of the energy difference is 80 meV rms, while the energy spread of each individual beam changes less than 1 meV.

V. SPECTROMETER RESOLUTION, BEAM EMITTANCE REQUIREMENT, AND PHOTOCATHODE SOLUTION

In order to precisely model the *e-e* interaction between the probe and reference beam from the cathode to the detector, a complete beam optics design, including the spectrometer with imaging optics, is required to define the beam trajectory and envelope. A first-order spectrometer design is illustrated in Fig. 2. The spectrometer consists of a double-focusing dipole magnet followed by two stages of magnifying imaging optics. The layout and main parameters of the spectrometer are summarized in Table II. The dipole bends the beam trajectory with a radius of 0.5 m and an angle of $\pi/2$. With tilted pole faces at both the entrance and exit, the beam is imaged in both x and y directions with a 1:1 magnification from the object plane (sample) to the first image plane. Since the beam spot size is only a few tens of nanometers on the first image plane, imaging optics is necessary to magnify the beam spot to match the point-spread function of the detector. Here, we choose two identical imaging stages. Each stage consists of a permanent-magnet-quadrupole triplet [39,41] which magnifies 16.0 times in the x (the horizontal and dispersion) direction and 4.0 times in the y direction. The design the PMQ triplet, including the position and strength of each magnet, is summarized in Table III.

TABLE II. Main parameters of the spectrometer.

Parameters	Values
Bending radius R	0.5 m
Bending angle	$\pi/2$
Dipole strength, B_0	0.374 kG
Pole-face tilt angle, β_1 and β_2	27.3°
Sample to dipole entrance, L_1	1.534 m
Dipole exit to first image plane, L_2	1.534 m
First to second image plane, L_3	0.15 m
Second image plane to detector, L_3	0.15 m

The horizontal beam size on the first image plane σ_x^{FW50} includes contributions from the dipole dispersion, the transverse beam size at the sample, and possible aberrations in imaging. Thus, σ_x^{FW50}/D is the upper bound of the beam energy spread, where D is the dispersion at the first image plane. In Fig. 9, we show the horizontal beam centroid x_0 and beam size σ_x^{FW50} on the first image plane for energy variation of -100 to 100 eV (-2×10^{-5} to -2×10^{-5} of 5 MeV) around the nominal value. The dispersion, i.e., the slope of the centroid curve, is $D = 0.37$ μm/eVσ_x^{FW50} is maintained around 32 nm, which corresponds to 85 meV. The electron-beam parameters are listed in Table I, except with $\Delta y = 0$ and $\Delta t = 0$, and the actual FW50 energy spread is $\delta E = 62$ meV. The results demonstrate that the spectrometer is capable of resolving <0.1-eV energy spread.

TABLE III. Parameters of the permanent magnet quadrupoles for a single triplet imaging stage. The object plane is at $z = 0$, and the image plane is at $z = 0.15$ m.

Name	Thickness	Gradient	Position
Q_1	6 mm	537.5 T/m	8.51 mm
Q_2	4 mm	−537.5 T/m	22.07 mm
Q_3	2 mm	537.5 T/m	28.92 mm

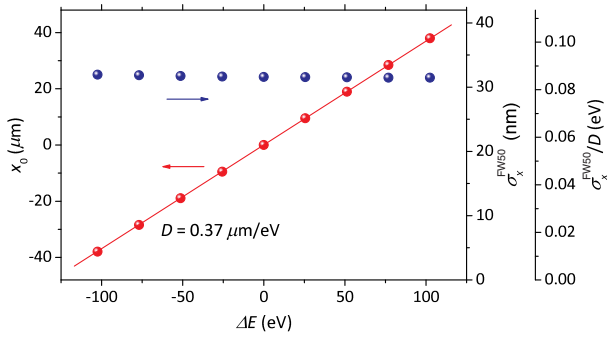

FIG. 9. At the first image plane, the beam centroid in the horizontal direction x_0 for beam energies off the nominal value by -2×10^{-5} to 2×10^{-5} or, roughly, -100 to 100 eV for 5-MeV beam energy. The beam size σ_x^{FW50} stays approximately 32 nm, which corresponds to 85 meV.

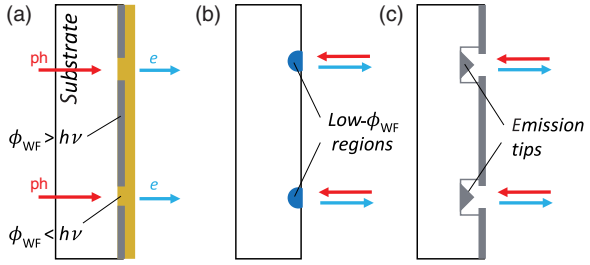

FIG. 10. Illustrations of the cathode concepts for the reference-beam technique. Two beams each with picometer-radian emittance can be generated with transverse and temporal separations from the photocathode. (a) Back-illuminated flat cathode with aperture masks to define the emission area. (b) Front-illuminated cathode with nanofabricated nanometer-size, low-work-function emission sites. (c) Laser-trigged photoemission nanotips. The red and blue arrows indicate the trajectory of the cathode drive laser and photoelectrons, respectively. There is time delay between the two laser pulses.

The undesired components in the horizontal beam size for energy spread determination, including contributions from the beam spot size at the sample and possible aberration in imaging, are related to the emittance of the electron beam. To allow characterization of a sub-0.1-eV energy spread with a dispersion of $D = 0.37$ μm/eV, the horizontal beam size needs to be less than 37 nm on the first image plane, hence, also at the object plane (sample location) with a 1:1 imaging. Meanwhile, the constrain we choose for the beam divergence at the sample $\sigma_{x'/y'}^{\mathrm{FW50}}$ is that it should be 1 order of magnitude smaller than the typical Bragg angle (approximately 1 mrad for 5-MeV electrons); thus, the divergence should be approximately 100 μrad or smaller. Combining the two aspects, the upper limit for the normalized FW50 beam emittance is 40 pm rad or, roughly, 25 pm rad with the rms definition.

It is a challenge but actually feasible to generate 25 pm rad or lower emittance from a photocathode. The intrinsic emittance is estimated to be 0.23–mm-mrad per millimeter rms emission size, which is dominated by the laser excitation bandwidth. The contribution from the cathode temperature is negligible, since the cathode is at cryogenic temperature in a SRF gun. The effects due to laser heating [50] can be minor if the laser fluence can be controlled at a miniature level of (0.1 mJ/cm^2). The required driving laser fluence is $F = N_e h\upsilon/\mathrm{QE}^{-1}A^{-1}$, where N_e is the average number of photoelectrons per pulse, $h\upsilon$ is the drive photon energy, the quantum efficiency $\mathrm{QE} = N_e/N_{\mathrm{ph}}$ is defined as the ratio between the numbers of photoelectrons and incident photons, and A is the emission area. For example, with $N_e = 0.5$, $h\upsilon = 4.5$ eV, $\mathrm{QE} = 1\times10^{-5}$, and $A = \pi(100\ \mathrm{nm})^2$ (rms size 50 nm), the drive laser fluence is $F = 0.12$ mJ/cm^2. The laser intensity is $I = F/\tau_{\mathrm{laser}} = 6.3$ GW/cm^2, where $\tau_{\mathrm{laser}} = 18.2$ fs is the laser-pulse duration. As the emission area A gets further reduced, a few effects should be considered, including whether the laser heating is strong enough to increase the intrinsic emittance, whether the absorbed I is less than a few tens of GW/cm^2 to avoid multiphoton emission and, hence, excessive energy spread of photoelectrons, and if the absorbed F is less than a few tens of mJ/cm^2 to avoid optical damage.

There are a few promising paths to reduce the emission area to approximately 100 nm or less to generate picometer radian emittance from a photocathode. The schematics of these concepts are illustrated in Fig. 10. First, it is feasible to directly focus the cathode driving laser to a spot size similar to its wavelength. With this approach, the final focusing optics needs to be very close (within a few millimeters) to the cathode surface; hence, a back-illuminated [52–55] and also high-gradient rf-field-compatible photocathode should be used. One step further, one can nanoengineer an aperture on the back side of the cathode to more precisely control the emission area, as shown in Fig. 10(a). Second, on a flat and uniform cathode surface assisted by electron- or ion-beam lithography, one can dope a small area to reduce the photoemission work function. Then, by tuning the laser wavelength, photoelectrons will be generated only from the doped area, as shown in Fig. 10(b). Third, one can engineer nanostructures to confine optical intensities to subwavelength sites through surface-plasmon effects, and photoemission will happen only at these high optical intensity regions [56,57], while the nanostructures may increase the geometric curvature of the emission surface and induce transverse rf electric fields, which both increase the intrinsic emittance. Finally, multiphoton emission or field-assisted single-photon emission from nanotips also provide nanometer source size and picometer-radian emittance [58–60]. However, above threshold, ionization should be avoided, which may otherwise broaden the initial energy spread to several electron volts. Considering the large local field enhancement close to the apex of the nanotips, the compatibility and robustness

of these tips with several tens of MV/m global gradient need to be experimentally explored and verified.

VI. EFFECTS OF ELECTRON-ELECTRON INTERACTIONS

In this section, we discuss how *e*-*e* interactions affect the energy resolution of the EELS measurement. The interactions between the probe and reference beams can potentially shift the average energy of each individual beam, i.e., introducing uncertainty in the *difference* between their energies $\delta|E_{\text{probe}} - E_{\text{ref}}|$. The interactions within each beam, if there contains more than one electron, significantly broadens the energy spread of the probe beam δE_{probe} and, hence, degrades the energy resolution.

We first consider the simplest case: when there is exactly one e in the probe beam and one e in the reference beam. It is straightforward to track the interaction between the two particles from the cathode to the detector. The "spacecharge3D" algorithm in GPT, which directly calculates relativistic point-to-point interactions is used. For each simulation run, we randomly generate one e within the defined phase space for the probe beam, and similarly, one e for the reference beam. The simulation is repeated multiple times to establish the statistics. The dependence of $\delta|E_{\text{probe}} - E_{\text{ref}}|$ on the initial transverse and temporal offsets Δy and Δt is shown in Fig. 11. $\delta|E_{\text{probe}} - E_{\text{ref}}|$ quickly decreases with larger Δy and Δt. We choose $\Delta y = 50\ \mu$m and $\Delta t = 0.5$ ps where the interaction between the single-e probe beam and single-e reference beam becomes negligible. Note that the result is not divergent as Δy and Δt are approaching zero, since both of the initial transverse and temporal beam sizes are finite rather than a point.

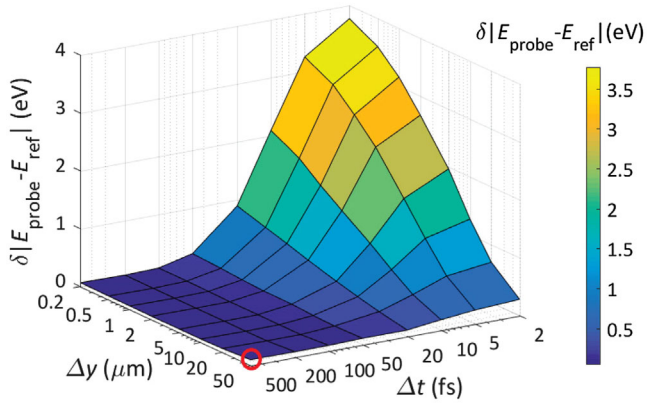

FIG. 11. Uncertainty of $E_{\text{probe}} - E_{\text{ref}}$ for different offsets Δy and temporal offsets Δt of the probe and reference beams, due to *e*-*e* interactions with exactly one e in the probe beam and one e in the reference beam. Other beam parameters are summarized in Table I. For each data point, 1000 simulation runs are performed to build up the statistics.

The probability that there are n electrons in the beam follows the Poisson distribution $P(n) = \lambda^n e^{-\lambda}/n!$, where λ is the average number of electrons per pulse. It is obvious that even when we choose λ equal to or less than 1, there is nonzero probability that the beam contains more than one e. When there are two e's in either the probe or reference beam, the main effect is a significant growth of the energy spread, while the average energies of the two beams stay approximately constant with offsets $\Delta y = 50\ \mu$m and $\Delta t = 0.5$ ps. The energy spread of a two-e beam can be calculated also in a straightforward way. In each simulation run, two particles are launched randomly within the initial phase space volume of a single beam and tracked from the cathode to the detector. The result can also be extrapolated from Fig. 11 by pushing both Δy and Δt to zero. The FW50 energy spread of a two-e beam is 3.3 eV with beam parameters listed in Table I.

We define the measurement efficiency as the percentage that the probe and reference beams both contain at least one e. The measurement efficiency is, thus, $[1 - P(0)]^2$ and can be well approximated by the first few dominating terms $[P(1) + P(2) + P(3)]^2$, as shown in Fig. 12(a).

The overall energy resolution of the EELS measurement is the weighted average over all possible combinations of beam charge, e.g., $1e$-$1e$, $1e$-$2e$, $2e$-$1e$, $2e$-$2e$…, for the probe and reference beams. As we discussed before, for the reference beam, only its average is relevant to the energy resolution, even if its energy spread grows when containing two or more e's. Thus, the energy resolution will be dominated by the energy spread of the probe beam. We summarize in Table IV the energy resolution δ_1, δ_2, and δ_3

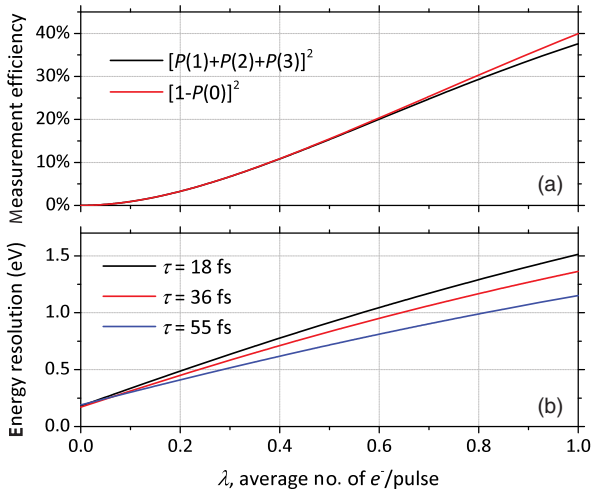

FIG. 12. (a) Measurement efficiency of the reference-beam technique due to the Poisson distribution of the number of electrons in the probe and reference beams. The exact efficiency $[1 - P(0)]^2$ can be well approximated by $[P(1) + P(2) + P(3)]^2$ for $\lambda < 1$. (b) Energy resolution δ as a function of λ. One can improve δ by relaxing the initial bunch length of the electron beam.

TABLE IV. Energy resolution δ_1, δ_2, and δ_3 when there are one, two, and three e^-'s in the probe beam, respectively. δ_1, δ_2, and δ_3 can be improved by lengthening the initial bunch length, however, at the cost of compromised temporal resolution.

Energy resolution (eV)	$\tau = 18$ fs	$\tau = 36$ fs	$\tau = 55$ fs
δ_1	0.18	0.17	0.19
δ_2	3.3	3.0	2.4
δ_3	4.1	3.5	3.1

when there are one, two, and three electrons in the probe beam, respectively. The overall energy resolution can be calculated as

$$\delta = \frac{\sum_n \delta_n P(n)}{\sum_n P(n)}, \tag{5}$$

and the result is shown in Fig. 12(b). In the limit of $\lambda \to 0$, δ is <0.2 eV and has no contribution from *e-e* interactions. As λ increases, the contributions from $P(2)$ and $P(3)$ become more significant and δ increases. One may wonder that if the final overall energy resolution target is notably larger than 0.1 eV, hence, no need to maintain the 0.1-eV measurement resolution in the spectrometer, is it worth increasing the initial spot size to reduce the effects of *e-e* interactions? This approach turns out to be not very effective. The reason is that the photoelectrons have 0.2-mrad divergence from the cathode; thus, the transverse beam size is soon (within a few hundreds of micrometers from the cathode) dominated by the divergence rather than the initial size. Instead, slightly increasing the initial pulse duration is more effective to reduce the *e-e* interaction-induced growth of δ. The reason is that the relative longitudinal particle motion is quickly frozen, and the longer initial pulse duration directly translates into larger spacing between particles. In Table IV and Fig. 12, we also show the results with 2 and 3 times longer drive laser-pulse duration, which improves the energy resolution by roughly 25%.

VII. SUMMARY AND DISCUSSION

In this paper, we present the concept and design a femtosecond EELS system based on a high-gradient, mulit-MeV energy photocathode rf gun. The tens of MV/m acceleration gradient and several-MeV output energy of the rf gun are critical to the generation of 10-fs bunch length, which enables a one-order-of-magnitude improvement of the temporal resolution beyond existing technologies. However, it is a challenge to reach electron-volt-level energy resolution, since the energy stability of the electron beams is at best 1×10^{-5} or 50 eV out of 5-MeV level with state-of-the-art rf amplitude and phase performance. To tackle the challenge, we propose a reference-beam technique which can effectively eliminate the effects of the rf instability.

With the reference-beam technique, we generate a pair of electron beams called the probe beam and reference beam each time from the cathode with controlled spatial and temporal separations. By properly choosing the beam and gun parameters, the energy *difference* between the two beams can be precisely controlled and become essentially immune to the rf jitter. Both beams are recorded by the spectrometer detector on a shot-by-shot basis. Only the probe beam interacts with samples and extracts the spectroscopic information of the dynamic process, and the average energy of the reference beam serves as the reference to the position of the zero-loss peak. We quantitatively study the requirements of the beam parameters, first-order spectrometer design, and the contribution to the energy resolution from the rf field and *e-e* interactions. Supported by detailed numerical modeling, we demonstrate the feasibility of achieving sub-electron-volt energy resolution and 10-fs-level temporal resolution.

It is worth pointing out that the required key hardware components to realize femtosecond MeV EELS are all under active R&D. It is promising that the assumed specifications used in our design can be available in the near future. For example, there is tremendous effort to improve the gradient of cw superconducting and normal-conducting guns from the current 20-MV/m level to >40 MV/m for future XFELs [61]. An ultrastable rf power source and rf-to-laser synchronization system is being developed for these facilities for better stability and temporal control. The key technologies for the high-speed detectors at these facilities can naturally benefit the development of the megahertz readout, single-electron sensitivity, micrometer spatial resolution detector for the spectrometer. Moreover, spectrometer detectors usually require >1000 pixels in the dispersion direction but a far fewer number of pixels in the vertical direction; therefore, the total of number of pixels is much less than two-dimensional imaging detectors, and it is less challenging to reach a higher readout rate.

A natural extension to the design presented in this paper is to further reduce the probe size to nanometer or even angstrom scale, which enables atomic level spatially column-by-column mapping of electronic dynamics. With an aberration-corrected spectrometer, one can tolerate much larger beam divergence, hence, much stronger focusing to form sharper probe size. At the same time, one should minimize the photoemission area and intrinsic divergence toward a transversely coherent electron source.

The requirements of the smallest possible pulse duration and energy spread are pushing the limit of the longitudinal emittance of the electron beam. Considering the uncertainty principle for time and energy $\Delta E \Delta t \geq \hbar/2$, with $\Delta E = 0.1$ eV FWHM, the lower limit for Δt is roughly 0.3-fs FWHM. One can approach this limit starting from better understanding and controlling the photoemission process. For a conserved longitudinal emittance, one should explore

rf, terahertz, and optical-based beam manipulation for generating attosecond pulse durations or milli-electron-volt energy spread tailored for various applications.

ACKNOWLEDGMENTS

The authors are grateful to P. Musumeci for helpful discussions. This work is supported in part by the U.S. Department of Energy Contract No. DE-AC02-76SF00515 and the SLAC UED/UEM Initiative Program Development Fund.

[1] R. F. Egerton, *Electron Energy-Loss Spectroscopy in the Electron Microscope*, 3rd ed. (Springer, New York, 2011).
[2] D. B. Williams and C. B. Carter, *Transmission Electron Microscopy—A Textbook for Materials Science*, 2nd ed. (Springer, New York, 2009).
[3] M. Chergui and A. H. Zewail, Electron and x-ray methods of ultrafast structural dynamics: Advances and applications, ChemPhysChem **10**, 28 (2009).
[4] R. J. D. Miller, Femtosecond crystallography with ultrabright electrons and x-rays: Capturing chemistry in action, Science **343**, 1108 (2014).
[5] Basic Energy Sciences Advisory Committee, Directing matter and energy: Five challenges for science and the imagination, 2007, https://science.energy.gov/~/media/bes/pdf/reports/files/Directing_Matter_and_Energy_rpt.pdf.
[6] Basic Energy Sciences Advisory Committee, Challenges at the frontiers of matter and energy: Transformative opportunities for discovery science, 2015, http://science.energy.gov/~/media/bes/besac/pdf/Reports/Challenges_at_the_Frontiers_of_Matter_and_Energy_rpt.pdf.
[7] P. Emma *et al.*, First lasing and operation of an ångstrom-wavelength free-electron laser, Nat. Photonics **4**, 641 (2010).
[8] T. Ishikawa *et al.*, A compact x-ray free-electron laser emitting in the sub-angstrom region, Nat. Photonics **6**, 540 (2012).
[9] C. Bostedt, S. Boutet, D. M. Fritz, Z. Huang, H. J. Lee, H. T. Lemke, A. Robert, W. F. Schlotter, J. J. Turner, and G. J. Williams, Linac coherent light source: The first five years, Rev. Mod. Phys. **88**, 015007 (2016).
[10] W. E. King, G. H. Campbell, A. Frank, B. Reed, J. F. Schmerge, B. J. Siwick, B. C. Stuart, and P. M. Weber, Ultrafast electron microscopy in materials science, biology, and chemistry, J. Appl. Phys. **97**, 111101 (2005).
[11] B. W. Reed, M. R. Armstrong, N. D. Browning, G. H. Campbell, J. E. Evans, T. LaGrange, and D. J. Masiel, The evolution of ultrafast electron microscope instrumentation, Microsc. Microanal. **15**, 272 (2009).
[12] A. H. Zewail, Four-dimensional electron microscopy, Science **328**, 187 (2010).
[13] G. Sciaini and R. J. D. Miller, Femtosecond electron diffraction: Heralding the era of atomically resolved dynamics, Rep. Prog. Phys. **74**, 096101 (2011).
[14] N. D. Browning, G. H. Campbell, J. E. Evans, T. B. LaGrange, K. L. Jungjohann, J. S. Kim, D. J. Masiel, and B. W. Reed, in *Handbook of Nanoscopy*, edited by G. Van Tendeloo, D. Van Dyck, and S. J. Pennycook (Wiley-VCH Verlag GmbH & Co. KGaA, Weinheim, Germany, 2012), Chap. 9.
[15] D. J. Flannigan and A. H. Zewail, 4D electron microscopy: Principles and applications, Acc. Chem. Res. **45**, 1828 (2012).
[16] P. Musumeci and R. K. Li, Femtosecond relativistic electron diffraction, ICFA Beam Dyn. Newslett. **59**, 13 (2012).
[17] Future of electron scattering and diffraction, Report of Basic Energy Sciences Workshop on the Future of Electron Scattering and Diffraction, 2014, http://science.energy.gov/~/media/bes/pdf/reports/files/Future_of_Electron_Scattering.pdf.
[18] P. Baum, Towards ultimate temporal and spatial resolutions with ultrafast single-electron diffraction, J. Phys. B **47**, 124005 (2014).
[19] F. Carbone, B. Barwick, O. H. Kwon, H. S. Park, J. S. Baskin, and A. H. Zewail, EELS femtosecond resolved in 4D ultrafast electron microscopy, Chem. Phys. Lett. **468**, 107 (2009).
[20] F. Carbone, O. H. Kwon, and A. H. Zewail, Dynamics of chemical bonding mapped by energy-resolved 4D electron microscopy, Science **325**, 181 (2009).
[21] L. Piazza, C. Ma, H. X. Yang, A. Mann, Y. Zhu, J. Q. Li, and F. Carbone, Ultrafast structural and electronic dynamics of the metallic phase in a layered manganite, Struct. Dyn. **1**, 014501 (2014).
[22] D. A. Plemmons, S. T. Park, A. H. Zewail, and D. J. Flannigan, Characterization of fast photoelectron packets in weak and strong laser fields in ultrafast electron microscopy, Ultramicroscopy **146**, 97 (2014).
[23] R. M. van der Veen, T. J. Penfold, and A. H. Zewail, Ultrafast core-loss spectroscopy in four-dimensional electron microscopy, Struct. Dyn. **2**, 024302 (2015).
[24] A. Feist, K. E. Echternkamp, J. Schauss, S. V. Yalunin, S. Schafer, and C. Ropers, Quantum coherent optical phase modulation in an ultrafast transmission electron microscope, Nature (London) **521**, 200 (2015).
[25] X. J. Wang, Z. Wu, and H. Ihee, Femto-seconds electron beam diffraction using photocathode rf gun, in *Proceedings of 2003 Particle Accelerator Conference*, Portland, OR, USA, 2003, p. 420, http://accelconf.web.cern.ch/AccelConf/p03/PAPERS/WOAC003.PDF.
[26] X. J. Wang, D. Xiang, T. J. Kim, and H. Ihee, Potential of femtosecond electron diffraction using near-relativistic electrons from a photocathode rf electron gun, J. Korean Phys. Soc. **48**, 390 (2006).
[27] J. B. Hastings, F. M. Rudakov, D. H. Dowell, J. F. Schmerge, J. D. Cardoza, J. M. Castro, S. M. Gierman, H. Loos, and P. M. Weber, Ultrafast time-resolved electron diffraction with megavolt electron beams, Appl. Phys. Lett. **89**, 184109 (2006).
[28] P. Musumeci, J. T. Moody, and C. M. Scoby, Relativistic electron diffraction at the UCLA Pegasus photoinjector laboratory, Ultramicroscopy **108**, 1450 (2008).
[29] R. K. Li, C. X. Tang, Y. C. Du, W. H. Huang, Q. Du, J. R. Shi, L. X. Yan, and X. J. Wang, Experimental demonstration of high quality MeV ultrafast electron diffraction, Rev. Sci. Instrum. **80**, 083303 (2009).

[30] Y. Murooka, N. Naruse, S. Sakakihara, M. Ishimaru, J. Yang, and K. Tanimura, Transmission-electron diffraction by MeV electron pulses, Appl. Phys. Lett. **98**, 251903 (2011).

[31] P. Zhu, Y. Zhu, Y. Hidaka, L. Wu, J. Cao, H. Berger, J. Geck, R. Kraus, S. Pjerov, Y. Shen, R. I. Tobey, J. P. Hill, and X. J. Wang, Femtosecond time-resolved MeV electron diffraction, New J. Phys. **17**, 063004 (2015).

[32] F. Fu, S. Liu, P. Zhu, D. Xiang, J. Zhang, and J. Cao, High quality single shot ultrafast MeV electron diffraction from a photocathode radio-frequency gun, Rev. Sci. Instrum. **85**, 083701 (2014).

[33] S. Manz, A. Casandruc, D. Zhang, Y. Zhong, R. A. Loch, A. Marx, T. Hasegawa, L. C. Liu, S. Bayesteh, H. Delsim-Hashemi, M. Hoffmann, M. Felber, M. Hachmann, F. Mayet, J. Hirscht, S. Keskin, M. Hada, S. W. Epp, K. Flottmann, and R. J. D. Miller, Mapping atomic motions with ultrabright electrons: Towards fundamental limits in space-time resolution, Faraday Discuss. **177**, 467 (2015).

[34] S. P. Weathersby *et al.*, Mega-electron-volt ultrafast electron diffraction at SLAC National Accelerator Laboratory, Rev. Sci. Instrum. **86**, 073702 (2015).

[35] M. Surman, P. Aden, R. J. Cash, J. A. Clarke, D. M. P. Holland, J. W. McKenzie, M. D. Roper, W. A. Bryan, D. A. Wann, P. D. Lane, and J. G. Underwood, Electron diffraction on VELA at Daresbury, in *Proceedings of IPAC 2014*, p. WEPRO108, http://accelconf.web.cern.ch/accelconf/IPAC2014/papers/wepro108.pdf.

[36] S. Setiniyaz, H. W. Kim, I.-H. Baek, J. Nam, M. Chae, B.-H. Han, B. Gudkov, K. H. Jang, S. Park, Y. U. Jeong, S. Miginsky, and N. Vinokurov, Beam characterization at the KAERI UED beamline, J. Korean Phys. Soc. **69**, 1019 (2016).

[37] D. Filippetto and H. Qian, Design of a high-flux instrument for ultrafast electron diffraction and microscopy, J. Phys. B **49**, 104003 (2016).

[38] J. Maxson, D. Cesar, G. Calmasini, A. Ody, P. Musumeci, and D. Alesini, Direct Measurement of Sub-10 fs Relativistic Electron Beams with Ultralow Emittance, Phys. Rev. Lett. **118**, 154802 (2017).

[39] R. K. Li and P. Musumeci, Single-Shot MeV Transmission Electron Microscopy with Picosecond Temporal Resolution, Phys. Rev. Applied **2**, 024003 (2014).

[40] D. Xiang, F. Fu, J. Zhang, X. Huang, L. Wang, X. Wang, and W. Wan, Accelerator-based single-shot ultrafast transmission electron microscope with picosecond temporal resolution and nanometer spatial resolution, Nucl. Instrum. Methods Phys. Res., Sect. A **759**, 74 (2014).

[41] D. Cesar, J. Maxson, P. Musumeci, Y. Sun, J. Harrison, P. Frigola, F. H. O'Shea, H. To, D. Alesini, and R. K. Li, Demonstration of Single-Shot Picosecond Time-Resolved MeV Electron Imaging Using a Compact Permanent Magnet Quadrupole Based Lens, Phys. Rev. Lett. **117**, 024801 (2016).

[42] J. C. Williamson and A. H. Zewail, Ultrafast electron diffraction. Velocity mismatch and temporal resolution in crossed-beam experiments, Chem. Phys. Lett. **209**, 10 (1993).

[43] X. J. Wang, X. Qiu, and I. Ben-Zvi, Experimental observation of high-brightness microbunching in a photocathode rf electron gun, Phys. Rev. E **54**, R3121(R) (1996).

[44] K. L. Jensen, N. A. Moody, D. W. Feldman, E. J. Montgomery, and P. G. O'Shea, Photoemission from metals and cesiated surfaces, J. Appl. Phys. **102**, 074902 (2007).

[45] L. Wu and L. K. Ang, Nonequilibrium model of ultrafast laser-induced electron photofield emission from a dc-biased metallic surface, Phys. Rev. B **78**, 224112 (2008).

[46] D. H. Dowell and J. F. Schmerge, Quantum efficiency and thermal emittance of metal photocathodes, Phys. Rev. ST Accel. Beams **12**, 074201 (2009).

[47] C. P. Hauri, R. Ganter, F. Le Pimpec, A. Trisorio, C. Ruchert, and H. H. Braun, Intrinsic Emittance Reduction of an Electron Beam from Metal Photocathodes, Phys. Rev. Lett. **104**, 234802 (2010).

[48] M. Aidelsburger, F. O. Kirchner, F. Krausz, and P. Baum, Single-electron pulses for ultrafast diffraction, Proc. Natl. Acad. Sci. U.S.A. **107**, 19714 (2010).

[49] L. Cultrera, S. Karkare, H. Lee, X. Liu, I. Bazarov, and B. Dunham, Cold electron beams from cryocooled, alkali antimonide photocathodes, Phys. Rev. ST Accel. Beams **18**, 113401 (2015).

[50] J. Maxson, P. Musumeci, L. Cultrera, S. Karkare, and H. Padmore, Ultrafast laser pulse heating of metallic photocathodes and its contribution to intrinsic emittance, Nucl. Instrum. Methods Phys. Res., Sect. A **865**, 99 (2017).

[51] General Particle Tracer (GPT), http://www.pulsar.nl/gpt/.

[52] N. Yamamoto, T. Nakanishi, A. Mano, Y. Nakagawa, S. Okumi, M. Yamamoto, T. Konomi, X. Jin, T. Ujihara, Y. Takeda, T. Ohshima, T. Saka, T. Kato, H. Horinaka, T. Yasue, T. Koshikawa, and M. Kuwahara, High brightness and high polarization electron source using transmission photocathode with GaAs-GaAsP superlattice layers, J. Appl. Phys. **103**, 064905 (2008).

[53] R. Inagaki, M. Hosaka, Y. Takashima, N. Yamamoto, T. Hitosugi, S. Shiraki, E. Kako, Y. Kobayashi, S. Yamaguchi, M. Katoh, T. Konomi, T. Tokushi, and Y. Okano, Development of multi-alkali photocathode deposited on $LiTi_2O_4$ substrate for SRF-gun, in *IPAC2014: Proceedings of the 5th International Particle Accelerator Conference, Dresden, Germany, 2014*, p. MOPRI035, http://accelconf.web.cern.ch/accelconf/ipac2014/papers/mopri035.pdf.

[54] H. Lee, L. Cultrera, and I. Bazarov, Intrinsic emittance reduction in transmission mode photocathodes, Appl. Phys. Lett. **108**, 124105 (2016).

[55] A. Căsăndruc, R. Bücker, G. Kassier, and R. J. D. Miller, Optical fiber-based photocathode, Appl. Phys. Lett. **109**, 091105 (2016).

[56] R. K. Li, H. To, G. Andonian, J. Feng, A. Polyakov, C. M. Scoby, K. Thompson, W. Wan, H. A. Padmore, and P. Musumeci, Surface-Plasmon Resonance-Enhanced Multiphoton Emission of High-Brightness Electron Beams from a Nanostructured Copper Cathode, Phys. Rev. Lett. **110**, 074801 (2013).

[57] A. Polyakov, C. Senft, K. F. Thompson, J. Feng, S. Cabrini, P. J. Schuck, H. A. Padmore, S. J. Peppernick, and W. P. Hess, Plasmon-Enhanced Photocathode for High Brightness and High Repetition Rate X-Ray Sources, Phys. Rev. Lett. **110**, 076802 (2013).

[58] D. Ehberger, J. Hammer, M. Eisele, M. Kruger, J. Noe, A. Hogele, and P. Hommelhoff, Highly Coherent Electron

Beam from a Laser-Triggered Tungsten Needle Tip, Phys. Rev. Lett. **114**, 227601 (2015).

[59] A. Feist, N. Bach, N. Rubiano da Silva, T. Danz, M. Möller, K. E. Priebe, T. Domröse, J. G. Gatzmann, S. Rost, J. Schauss, S. Strauch, R. Bormann, M. Sivis, S. Schäfer, and C. Ropers, Ultrafast transmission electron microscopy using a laser-driven field emitter: Femtosecond resolution with a high coherence electron beam, Ultramicroscopy **176**, 63 (2017).

[60] M. Müller, V. Kravtsov, A. Paarmann, M. B. Raschke, and R. Ernstorfer, Nanofocused plasmon-driven sub-10 fs electron point source, ACS Photonics **3**, 611 (2016).

[61] Future of electron sources, Report of the Basic Energy Sciences Workshop on the Future of Electron Sources, 2016, https://science.energy.gov/~/media/bes/pdf/reports/2017/Future_Electron_Source_Worskhop_Report.pdf.